EE

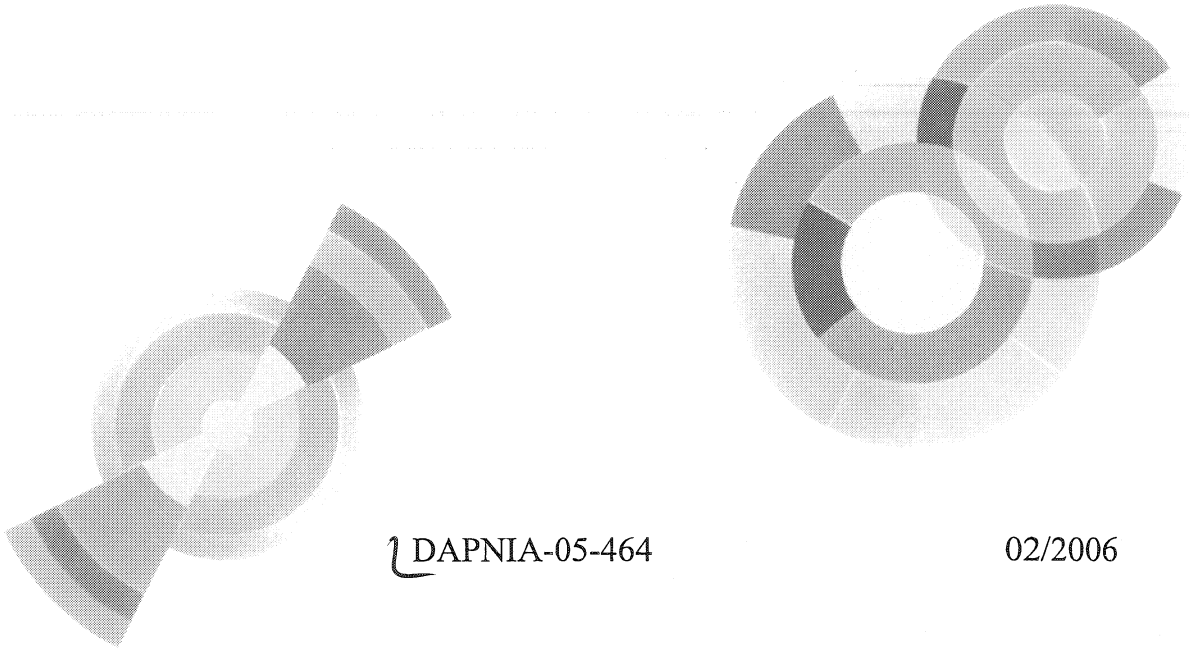

DAPNIA-05-464 02/2006

Neutron Production in Semiprototypic Target Assemblies for Accelerator Transmutation Technology

G.L. Morgan et al
(J. Frehaut, X. Ledoux, S. Leray, E. Petitbon)

Nuclear Science and Engineering, 151, 293-304 (2005)

Département d'Astrophysique, de Physique des Particules, de Physique Nucléaire et de l'Instrumentation Associée

DSM/DAPNIA, CEA/Saclay F - 91191 Gif-sur-Yvette Cédex
Tél : (1) 69 08 24 02 Fax : (1) 69 08 99 89
http : //www-dapnia.cea.fr

NUCLEAR SCIENCE AND ENGINEERING: **151**, 293–304 (2005)

Neutron Production in Semiprototypic Target Assemblies for Accelerator Transmutation Technology

G. L. Morgan, K. R. Alrick, D. W. Bowman, F. C. Cverna, N. S. P. King, and P. E. Littleton

Los Alamos National Laboratory, Los Alamos, New Mexico 87545

G. A. Greene,* A. L. Hanson, and C. L. Snead, Jr.

Brookhaven National Laboratory, Upton, New York 11973

J. M. Hall

Lawrence Livermore National Laboratory, Livermore, California 94551

J. Frehaut, X. Ledoux, S. Leray, and E. Petibon

Commissariat a l'Energie Atomique, Saclay, France

R. T. Thompson

Bechtel Nevada, Los Alamos, New Mexico 87545

P. D. Ferguson

Oak Ridge National Laboratory, Oak Ridge, Tennessee 37831

and

E. A. Henry and T. E. Ward

U.S. Department of Energy, Washington, D.C. 20585

Received February 26, 2004
Accepted January 14, 2005

Abstract – *Integral neutron production was measured by the manganese-activation technique, on targets semiprototypic of spallation-neutron-driven transmutation systems, after irradiation by 400-MeV to 2.0-GeV protons. The purpose of these experiments was to provide data to benchmark nuclear transport codes for targets irradiated by protons in this energy range, as well as to evaluate design options to maximize the production of spallation neutrons in various targets under consideration. These computer codes are used to design accelerator systems that will utilize spallation neutrons for the generation of tritium, transmutation of nuclear waste, production of radioisotopes, and other scientific investigations. Some of the targets used in this investigation were semiprototypic of the proposed Accelerator Production of Tritium target. Other targets were included to provide data to test the computational models in the codes. Total neutron production is the main factor that determines the economics of transmutation for a particular accelerator design. Comparisons of the data reported here with calculations from computer simulations show agreement to within 15% over the entire energy region for most of the targets.*

*E-mail: greene@bnl.gov

I. INTRODUCTION

In recent years, several facilities have been proposed to utilize spallation neutrons. They include the Accelerator Production of Tritium (APT) in the United States and TRISPAL in France, the Accelerator Transmutation of Waste, the Advanced Fuel Cycle Initiative, and the Spallation Neutron Source. A key factor in the design of an accelerator-driven transmutation (ADT) system is the neutron production and transport in the target/blanket system. In these systems, the target is the material being irradiated by the proton beam that generates the spallation neutrons. A blanket generally surrounds the target and contains the material with which the neutrons interact. Nuclear transport codes such as the MCNPX code[1] and the LAHET code system[2] (LCS), two of the computational tools used in these designs, track the interactions of the incident particles along with any subsequent particles.

In developing a transmutation system, it is important that data are obtained to benchmark the ability of these codes to predict the neutronics of the proposed target designs. Therefore, these experiments studied neutron production per incident proton in several assemblies with dimensions and compositions similar to likely candidates for ADT targets. In the experiments reported in this paper, 400-MeV to 2-GeV protons were used to irradiate the spallation targets.

This work extends earlier studies of spallation neutron production[3] by including a wider range of incident proton energy along with additional materials and target configurations. Four target materials were selected: lead, tungsten, iron, and lithium. Some target materials were arranged differently, such as solid versus split tungsten disks, and some targets had different diameters. Finally, the proton energy was varied for most targets. The measurements were carried out using the manganese-activation technique, so the measurements of neutron production are actually inferred from the measured activation of the manganese. The measurements of ^{56}Mn production, used to infer the number of neutrons generated per incident proton, are compared with calculations using the LCS-2.8.3/MCNP-4B and MCNPX-2.5.D (a beta test version of MCNPX) computer codes. Some of the measurements were made at the Los Alamos Neutron Science Center (LANSCE) accelerator at the Los Alamos National Laboratory (LANL), and the others were performed at the SATURNE accelerator at Commissariat à l'Energie Atomique (CEA/Saclay). Frehaut et al.[4] made a detailed independent analysis of the experiments performed at SATURNE.

II. EXPERIMENTAL PROCEDURE

II.A. Target/Moderator System

To facilitate the study of these targets, a standard design was adopted that required that all the target assemblies fit inside a 10-in. schedule-60 aluminum pipe, 3.35 m long. This pipe could then be placed inside a lead blanket, of 2.00-m length × 60-cm outside diameter. This blanket provided some neutron multiplication through (n, xn) reactions, which also shifted the neutron spectra to lower energies. The lower-energy neutron spectra resulted in lower leakage of neutrons from the system.

In the manganese-activation technique, neutrons produced in the target/blanket are moderated and captured in a large volume of water containing $MnSO_4$ in solution. Calculations show that the capture efficiency of this system is >99% for neutrons <20 MeV. Approximately 2% of the thermalized neutrons that are captured form ^{56}Mn, which has a half-life of 2.5785 ± 0.0006 h and emits an 846.812-keV gamma ray with a branching ratio of 98.9 ± 0.3%. The thermal neutron capture cross section of manganese as well as those of the other materials present (mainly aluminum, hydrogen, oxygen, carbon, and lead or tungsten) is accurately known and does not contribute appreciably to the uncertainty of the computer simulations of the fraction of neutrons captured in the manganese. Most of the other thermal neutrons are captured in the hydrogen in the water.

To use this technique, a water tank with dimensions of 2.5-m diameter and 3.0-m length surrounds the target/blanket assembly as shown in Fig. 1. The tank was constructed in three sections for ease of handling. The upper section contained only water, so it could be drained and removed to permit opening of the blanket and changing of the target. The two lower sections contained a solution of 1 to 2% $MnSO_4$. While this arrangement compromised the symmetry of the experiment, it was necessary to ensure that the target could be changed without spilling any water containing radioactive ^{56}Mn. The total volume of the water in the upper tank was 5047 ℓ, and the volume of the $MnSO_4$ solution in the two lower tanks was 9245 ℓ.

Calculations showed that most of the ^{56}Mn is produced near the target, so the $MnSO_4$ solution had to be mixed thoroughly before taking a sample for counting to determine the total ^{56}Mn production accurately. Mixing was accomplished with a circulation system using two pumps, each of which removed water from the outer region of one section and injected it into the central region of the other section through a pipe running the length of the tank. The system had a series of orifices designed to maximize mixing. A high-resolution germanium detector was mounted in a shielded box in contact with one of the circulation pipes ~3 m from the tank to monitor the ^{56}Mn activity in the circulating water after an irradiation. This allowed verification that the water was completely mixed by observing that the decrease in the activity in the line accurately tracked the half-life of ^{56}Mn.

Most of the experiments were conducted at the SATURNE accelerator at CEA/Saclay while the rest were conducted at the LANSCE accelerator at LANL. Proton beams at SATURNE could have energies up to 3 GeV

Fig. 1. Photograph of the target/moderator system with the water storage tanks in the background. The upper section of the moderator tank has been removed to reveal the lead blanket resting in the lower two sections of the moderator tank.

and intensities of about 10^{12} particles per spill. Proton beams exited the beamline through a thin stainless steel window and entered the target assembly after passing through ~1 m of air. The LANSCE accelerator can provide higher intensity, but the proton energy is limited to a maximum of 800 MeV. Details of the target, blanket, and moderator assemblies are shown in Figs. 2, 3, and 4. As shown in Fig. 2, the blanket and moderator tanks contained tubes parallel to the direction of the proton beam at various radial positions to allow installation of activation foils and ^{3}He capsules to map the differential thermal neutron flux and isotope production. These measurements will not be discussed in this paper.

The set of targets used in these experiments included 10- and 25-cm-diam lead, 10- and 15-cm-diam tungsten, 25-cm-diam lithium (enriched in ^{7}Li), and

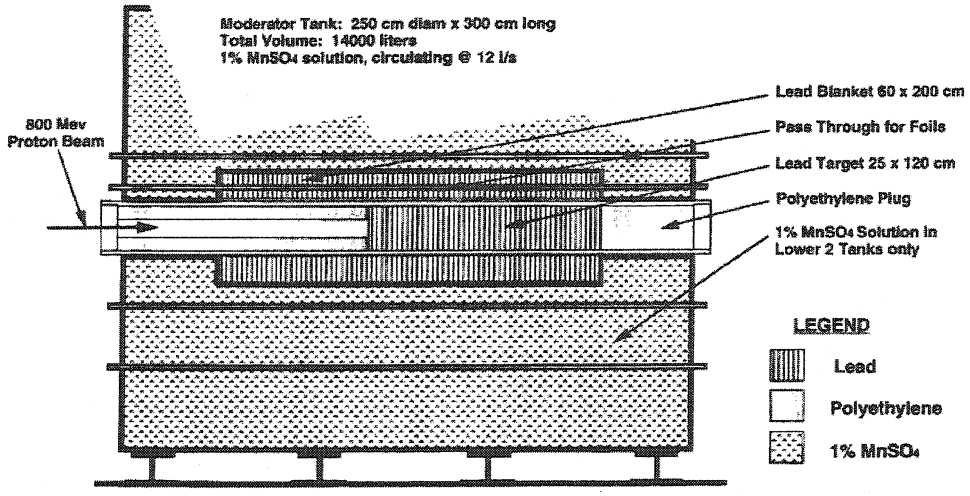

Fig. 2. Cross section of the target/moderator assembly showing the target tube with the solid lead target, the lead blanket surrounding the target, and the water moderator surrounding the target/blanket system.

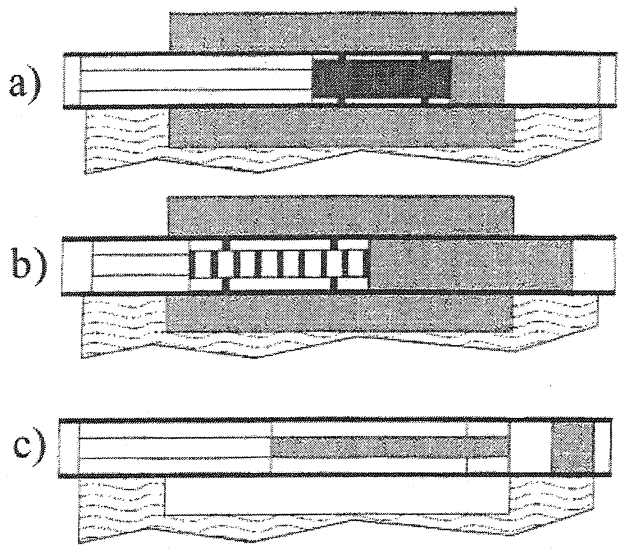

Fig. 3. Schematic diagrams of the various target configurations: (a) the solid tungsten target, (b) the separated tungsten target, and (c) the 10-cm-diam targets (W, Pb, and Fe) without the lead blanket.

10-cm-diam iron. Most were solid with the exception of two of the three tungsten targets, which had spaces between the tungsten disks (i.e., the split geometry). The 10-cm-diam tungsten target was in a split arrangement. One of the 15-cm-diam tungsten targets had a split geometry, while the other was solid. Those tungsten targets that were assembled in the split geometry were so arranged in order to represent the proposed design of the APT spallation target that was to have gaps between its tungsten rod bundles to enhance neutron leakage from the target. The lead and tungsten targets were selected since they were candidate materials for the spallation targets in APT. The lithium and iron targets were chosen for validation of the computational models.

Figure 2 illustrates the solid 25-cm lead target mounted in the tank with the lead blanket. Since this target had the simplest design and was the one studied the most, it was considered the base case, and many discussions refer to it as such. It was 1.2 m long (the stopping length for protons at 800 MeV is ~40 cm; at 2 GeV it is ~1.2 m). The front of the lead target was 20 cm upstream of the centerline of the system. Any additional lead behind the stopping length served to scatter and multiply the forward-moving high-energy neutrons produced in the primary interaction region. The region upstream of the lead was filled with a 25-cm-diam annular high-density polyethylene (HDPE) cylinder with a 10-cm-diam hole on center providing an entrance for the proton beam. Additionally, the downstream end of the target pipe was blocked with a length of solid HDPE, 50 cm long and 25 cm in diameter. This backstop served as downstream shielding of high-energy neutrons and provided a mock continuation of the water bath surrounding the lead blanket. This target was irradiated by 0.4-, 0.8-, 1.6-, and 2.0-GeV protons.

The 10-cm-diam lead target was used to test the ability of the codes to calculate the proper divergence of the beam through the target. To perform this test, the lead blanket was removed from the tank, and the target was irradiated by 800-MeV and 2.0-GeV protons. For a complete comparison, the 25-cm-diam lead target was also irradiated with and without the lead blanket at these two energies. In effect, irradiations were performed on 10-, 25-, and 60-cm-diam lead targets. The 10-cm target, shown in Fig. 3c, was 1.40 m long, and most of it was mounted in a 4-in. aluminum tube that had ribs welded onto it to position it inside the 10-in. pipe. The last 25-cm length of this lead target was embedded in a 25-cm-diam cylinder of HDPE. This target was followed by 50 cm of 25-cm-diam HDPE. With this design, neutrons were generated only in the target. Protons that might escape the target would only interact with low-Z materials (mostly water and aluminum).

One of the 15-cm-diam tungsten targets was solid (Fig. 3a), and the other was split (Fig. 3b). Both were mounted inside a 6-in. inside diameter × 0.25-in. wall aluminum tube. Each tube had two nylatron rings around them to center them inside the 10-in. pipe. The solid tungsten target (Fig. 3a) consisted of 30 plates, each of which was 2.54 cm thick and was contained in tubing 81.3 cm long. It was followed by a lead backstop, 25 cm in diameter and 34.5 cm in length. Finally, there was 50 cm of 25-cm-diam HDPE. The upstream portion of the target was filled with a 1.32-m length of HDPE cylinders with 10-cm-diam holes on center. The proton beam entered through this opening. This target was irradiated by 0.4-, 0.8-, 1.6-, and 2.0-GeV protons.

The split tungsten target assembly (Fig. 3b) was arranged in a configuration of nine plates; each plate was 2.5 cm thick and was separated by a 10-cm air gap. The assembly was followed by a 25-cm-diam lead backstop 1.19 m long and then by a solid 25-cm-diam HDPE backstop 37.8 cm long. The upstream area was filled with the annular HDPE, 57.2 cm long. This target was irradiated by 0.8-, 1.2-, 1.6-, and 2.0-GeV protons.

The lithium target was 25 cm in diameter and 1.75 m long. It consisted of seven welded, thin-walled stainless steel cans filled with lithium enriched with ^{7}Li. The ^{7}Li content averaged 97.88%, ranging from a low of 97.78% to a high of 97.99%. In modeling this target for simulation, each can was explicitly modeled to represent the correct ^{7}Li and ^{6}Li content. The cylindrical wall of each can was 1.51 g/cm^2 thick, and the faces were 1.73 g/cm^2 thick. Since lithium is a low-Z material, 1.75 m of lithium is the stopping length for 400-MeV protons, so that was the only proton energy used with this target. This target included a 25-cm-diam × 25-cm-long lead backstop

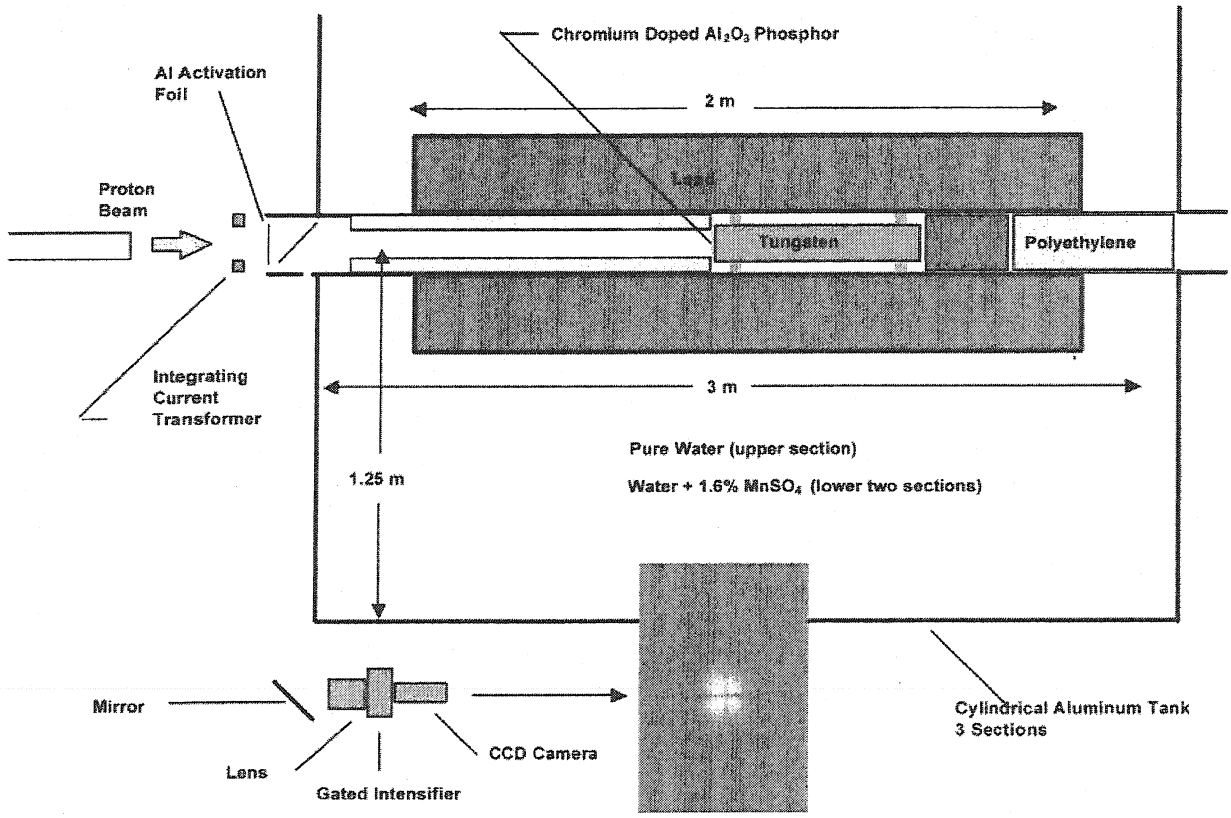

Fig. 4. Schematic diagram of the target/moderator system with the solid tungsten target emphasizing the systems used for beam monitoring.

followed by a 25-cm-diam × 50-cm-long HDPE backstop. The upstream annular HDPE was 50 cm long.

The 10-cm-diam tungsten target was arranged in a split geometry. The first two plates were 1 cm thick, the second pair was 2 cm thick, and the third pair was 3 cm thick. Each plate was enclosed in an aluminum can with a spacing of 15 cm between the cans. The plates were mounted in an 8-in. × 0.25-in. wall aluminum tube. The target was mounted on standoffs that fit into the 8-in. tube. This inner tube was filled with a $^3He/H_2$ mixture of 8.832 mol of ^3He and 0.118 mol of H_2. This target had a 25-cm-diam × 30.6-cm-long lead backstop. Water flowed in the gap between the 8-in. tube and the 10-in. pipe. Both tubes were welded at the two end plates. No HDPE was used in this target.

The last target was a 10-cm-diam iron target, 1.10 m long and similar in design to the 10-cm-diam lead target of Fig. 3c. It had a backstop of 10-cm-diam × 30-cm-long lead encased in an HDPE cylinder 25 cm in diameter × 25 cm long. This was followed by a solid 25-cm-long HDPE cylinder and then a 25-cm-long lead backstop. The front annular HDPE was 1.10 m long. This target was irradiated without the lead blanket.

The first two columns of Table I show the test matrix of targets and proton energies. The $MnSO_4$ solution varied between sets of measurements, so its concentration is specified in column 3. The targets that were irradiated without the lead blanket are denoted by "without blanket." All other targets had the lead blanket and are denoted by "with blanket." Design studies using LCS and MCNPX indicated that for a system of this size, the maximum neutron leakage from the moderator tank would be $<1\%$ for most of the configurations that used the lead blanket. For those targets for which the lead blanket was not used, calculated neutron losses were in the 1.2 to 5.0% range.

II.B. Beam Monitoring

Calculations showed that because the $MnSO_4$ solution was only in the two lower sections, a 5-cm vertical displacement of the proton beam from the center of the target would cause a 15% change in ^{56}Mn production. Therefore, the proton beam had to be positioned accurately. This was accomplished by imaging the proton beam spot on the front face of the target. This imaging system is shown schematically in Fig. 4. The imaging system consisted of a chromium-doped aluminum-oxide phosphor, indexed and accurately mounted on the front of the target. A thin aluminized Mylar pellicle reflected

TABLE I

Summary of the Experimentally Measured Values of ^{56}Mn Production per Proton Including Default MCNPX and LCS Code Calculations*

Target	Proton Energy (GeV)	$MnSO_4$ (wt%)	$^{56}Mn/p$ (p from ^{24}Na measurements)	$^{56}Mn/p$ (p from ^{22}Na measurements)	$^{56}Mn/p$ Experiment, Weighted Average	Uncertainty (%)	$^{56}Mn/p$ from LCS	Ratio Experiment/ LCS (LBIP)	$^{56}Mn/p$ from MCNPX	Ratio Experiment/ MCNPX (MBIP)
Solid 25 cm lead with blanket	0.4	0.833	0.0516	0.0475	0.050	3.8	0.048	1.04	0.052	0.96
	0.8	0.833	0.1726	0.1694	0.171	3.3	0.172	1.00	0.177	0.97
	0.8[a]	0.994	0.2046	—	0.205	4.3	0.205	1.00	0.211	0.97
	0.8	1.647	0.3355	0.3333	0.335	3.7	0.337	0.99	0.347	0.97
	1.6	1.647	0.8360	0.8766	0.855	3.1	0.823	1.04	0.846	1.01
	2.0	0.833	0.5735	0.5796	0.576	3.3	0.533	1.08	0.548	1.05
Solid 15 cm tungsten with blanket	0.4	1.647	0.0599	0.0545	0.059	3.9	0.062	0.95	0.066	0.89
	0.8	1.647	0.2064	0.1995	0.202	2.8	0.216	0.94	0.220	0.92
	1.6	1.647	0.5259	0.5156	0.519	2.7	0.520	1.00	0.535	0.97
	2.0	1.647	0.6837	0.6585	0.669	3.2	0.664	1.01	0.680	0.98
Split 10 cm tungsten with blanket	0.5[b]	0.822	0.0483	—	0.048	3.9	0.051	0.94	0.054	0.89
	0.8[a]	0.994	0.1255	—	0.126	4.4	0.136	0.93	0.140	0.90
Split 15 cm tungsten with blanket	0.8	1.647	0.2780	0.2786	0.278	2.8	0.341	0.82	0.303	0.92
	1.2	1.647	0.4842	0.5103	0.500	3.0	0.591	0.85	0.530	0.94
	1.6	1.647	0.6698	0.6978	0.688	2.8	0.824	0.83	0.741	0.93
	2.0	1.647	0.8239	0.8482	0.840	2.8	1.042	0.81	0.946	0.89
Solid 25 cm lead without blanket	0.8	1.647	0.3388	0.3365	0.337	3.0	0.347	0.97	0.360	0.94
	2.0	1.647	0.9484	0.9410	0.944	3.1	1.038	0.91	1.067	0.88
Solid 10 cm lead without blanket	0.8	1.647	0.2859	0.2749	0.279	2.9	0.320	0.87	0.329	0.85
	2.0	1.647	0.6879	0.6695	0.679	3.4	0.874	0.78	0.895	0.76
Solid 10 cm iron without blanket	0.8	1.647	0.1520	0.1479	0.150	10.4	0.122	1.23	0.120	1.25
Solid 25 cm lithium with blanket	0.4[a]	0.994	0.0458	—	0.046	4.8	0.036	1.28	0.054	0.85

*MCNPX default model for particle transport is the Bertini-ISABEL model with preequilibrium.
[a]Ref. 3.
[b]Ref. 9.

the light from this phosphor into a lens system, onto a mirror, and then into a shielded camera system. This camera system contained a wavelength filter to help remove stray light, a gated image intensifier, and a charge-coupled-device (CCD) video camera. This system provided real-time observation of the size and position of the proton beam. The images were recorded to analyze the intensity profile of the beam during the irradiation. The inset in Fig. 4 shows a typical beam spot. The index marks on the phosphor indicate 1-cm increments. The image was displayed on a monitor in the control room to quickly correct any diffuse or dislocated beam spots. To minimize the effects of any dislocation of the beam, the initial beam tuning was carried out using beam intensities reduced by a factor of 100 and continued for less than ~5 min at the beginning of an irradiation. In all cases, the beam spot was maintained within 2 mm of the target center and focused to a diameter of <2 cm full-width at half-maximum. Optical surveys before the experiment established that the axis of the target was on the axis of the proton beamline to within 2 mm.

Figure 4 also shows the systems used to monitor the total number of protons incident on a target during an irradiation. The primary method employed a stack of three aluminum foils, for which activation cross sections are accurately known in the energy range between 400 MeV and 2.0 GeV (Ref. 5). Secondary checks on the integrated proton fluence were made using other beam diagnostics.

One involved using an integrating current transformer (ICT) (Bergoz Model 122:70:5) that can respond to beam pulses as short as 1 ns and can produce an output pulse ~20 ns wide with a charge proportional to the charge of the beam. To use this technique, the radio-frequency (rf) power to the SATURNE accelerator was left on, which bunched the extracted beam into bunches ~20 ns wide and 400 ns apart (depending on proton energy). The signal from the ICT for each bunch was amplified and gated into an integrate-and-hold circuit (Bergoz Model BCM-IHR). The integrated output was sampled by an analog-to-digital convertor at the end of each extraction and stored in a histogram as well as in an array of points for each accelerator cycle. The total charge was determined by calculating the weighted sum of this histogram. Additionally, if there were large fluctuations or interruptions in the beam, the measured aluminum and manganese activities could be corrected for the nonuniformity of the irradiation using the time-dependent data from the other array. The system was calibrated using the techniques described in Ref. 5. The deviation between the beam charge determined with the ICT and aluminum activation averaged 20%. This difference was attributed to the loss of beam signals from the ICT due to weak pulses and erratic extraction.

For the last series of experiments on the separated tungsten target, a phosphor viewed by a photomultiplier tube was used. The signal from the photomultiplier was integrated over each extraction cycle and again was stored in the same histogram and array as the ICT. The accelerator rf was off, and extraction was continuous instead of bunched. At each energy, the measured proton fluence was corrected for the relative stopping power of the phosphor material for protons. This system had no absolute calibration and served only as a relative measurement to compare to the aluminum activation measurements.

II.C. Irradiation Procedure

At the start of each experiment, a fresh stack of aluminum foils was mounted in the beam in front of the target assembly, and the circulation pumps were started. The ICT or phosphor system and associated electronics were calibrated. The imaging system and the data acquisition computer for the current monitor system were enabled. Low-intensity beam delivery was begun, and the time was recorded. As soon as the beam was on target, the operators observed the beam spot with the imaging system and adjusted the primary transport to center and focus it. The beam intensity was then increased to full intensity, and that time was recorded. A typical irradiation for the lead target lasted ~30 min at a time-averaged beam current of 50 nA. At the end of the irradiation, the time was recorded, and a series of short counts was begun with the gamma-ray detector on the circulation line. The circulation pumps were run for at least 45 min, and then two 50-ml samples of the $MnSO_4$ solution were extracted from the system and placed in polyethylene bottles to count their activity. The gamma-ray detector on the circulation line continued to operate in order to track the decay of the ^{56}Mn. The measured activities were corrected for decay during and after the irradiation and scaled to the total volume of water in the moderator system to determine the total number of ^{56}Mn atoms produced. The middle aluminum activation foil was removed from the stack, and its ^{24}Na activity was measured to determine the total proton fluence on the target.

As indicated in Table I, the $MnSO_4$ concentration was varied from 0.82 to 1.65 wt%. These concentrations were very dilute solutions since $MnSO_4$ is ~50% soluble in water at room temperature. In both this work and in Ref. 3, the $MnSO_4$ concentration was very stable, as confirmed by chemical analysis at times separated by several months. Two independent determinations of the concentration were made. Chemical analyses had uncertainties of 1%. A second determination was made by weighing the $MnSO_4$ [the $MnSO_4$ was determined by chemical analysis to have one water of hydration (0.998 ± 0.001)] that was put into solution and using the total volume of water determined as described below. The agreement between the two measurements was within the estimated uncertainties, and the overall estimated uncertainty was 1%. For the dilute solutions used in this work, ^{56}Mn production is a linear function of

concentration; therefore, the uncertainty in concentration was included in the overall experimental uncertainty.

II.D. Determination of ^{56}Mn Activity

The $MnSO_4$ samples removed after the irradiation were counted with a germanium detector. An efficiency curve for this detector was determined by a series of calibrated gamma-ray sources. However, the principal calibration in absolute activity was obtained using a calibrated ^{54}Mn solution of nominal 50-ml volume in a polyethylene bottle identical to those used for the ^{56}Mn analyses. The gamma-ray energy from the decay of ^{54}Mn is 835.826 keV, or only ~10 keV below the gamma-ray energy from the decay of ^{56}Mn. The half-life of ^{54}Mn is 312.20 days, and it has a branching ratio of 99.975%. Therefore, the efficiency of the detector for a 50-ml solution containing ^{56}Mn could be determined by directly comparing the counting rates to the calibrated source of ^{54}Mn. Only a small correction (~1%) was necessary to compensate for the difference in the efficiency of the detector for detecting gamma rays from ^{54}Mn and ^{56}Mn. This correction was made using a log-log interpolation of the measured efficiency curve.

There were four parts to the uncertainty analysis of the ^{56}Mn activity in the total system. First was the statistical uncertainty in counting and in determining the peak area in the germanium detector measurement (~1%). Second was the uncertainty in the activity of the ^{54}Mn calibration source (2% as certified by the CEA/LMRI for source No. 4866/3). Third was the systematic uncertainty in the ratio of the sample volume to that of the total water in the two lower sections of the tank containing the $MnSO_4$ solution. The sample volumes were determined by weighing and had negligible uncertainty. The uncertainty of the volume of the total system was determined to 1% by measuring the volume of water removed from the holding tanks during the fill operation. This was done by carefully measuring the difference in the height of the water before and after filling, along with careful measurements of the dimensions of the tanks at several different heights. Finally, there was the correction for the residual activity in the $MnSO_4$ solution from the preceding irradiation. This correction was calculated using the activity measured for the preceding irradiation and the half-life of ^{56}Mn and was usually small since the irradiations were at least 8 h apart. The uncertainty in this correction was estimated to be 5%. These uncertainties were squared and added in quadrature to yield an overall uncertainty in the total amount of ^{56}Mn produced during an irradiation (see Table II). For the first set of measurements at SATURNE that included all the target configurations except the split tungsten target, all of the $MnSO_4$ solution samples were counted with a single detector. For the second set of measurements (on the split tungsten target), a second detector from LANL independently counted each sample.

TABLE II

Summary of the Various Factors Contributing to the Systematic Uncertainties of the Measurement

Source of Error	Magnitude of Error (%)
Circulating water volume	1
$MnSO_4$ concentration	1
^{56}Mn counting efficiency	2
Proton fluence determination	2 to 3
Background correction	5 (of background fraction)
Total systematic uncertainty (without background)	3 to 4

II.E. Determination of Total Proton Fluence Using Aluminum Activation

The center foil was removed from each aluminum foil stack and counted to determine its activity. The upstream and downstream foils served to ensure that the center foil was in equilibrium with the forward and backward recoiling spallation products. The aluminum foils were certified by the vendor to have purity >99.999%, and their dimensions were 10 cm square × 0.3 mm thick (~80 mg/cm^2). The dimensions of each foil were measured to ±0.1 mm, and they were weighed to ±1 mg (total mass ~8 g) to determine their areal density. The uniformity in the thickness of the foils was checked by measuring the foils at several points; uniformity was better than 1%. The determination of the aluminum foil thickness had an overall uncertainty estimated to be less than 0.5%.

The total proton fluence for each irradiation was calculated by counting two different activities in the aluminum. The first was the ^{24}Na activity that has a 14.9590-h half-life with a decay generating a 1368.598-keV gamma ray with a branching ratio of 100%. The center foil of each three-foil stack was counted using a germanium detector. The efficiency of the detector was determined using calibrated ^{60}Co sources since this gives two gamma rays with energies of 1173.237 and 1332.501 keV with branching ratios of 99.90 and 99.9824%, respectively. As with the ^{56}Mn counting, the efficiency of the detector for the gamma rays from ^{24}Na could be accurately extrapolated from that for the ^{60}Co source since the energy difference is only 36 keV. The source-to-detector distance was ~50 cm, sufficient to ensure that the efficiency for counting the 2-cm-diam activated spot was essentially the same as that for a point source. The total number of ^{24}Na atoms produced by the irradiation was then determined by correcting the measured activity for

decay from the time at the end of irradiation and for decay during the irradiation.

When the detectors were calibrated at CEA/Saclay, a ^{60}Co source supplied by CEA/Saclay was used. The efficiencies of the detectors were again measured at LANL with two different calibrated ^{60}Co sources: the first an Amersham source (ID 2U125) with a quoted uncertainty of 1.9% and the second an Amersham Mixed Radionuclide Standard (ID 2514QB) with a quoted uncertainty of 0.8%. The counting rates for these two standards agreed with the quoted activities to within 1%. The measured efficiencies as determined at CEA/Saclay and LANL agreed to within the expected uncertainties.

A second determination of the incident proton fluence was based on the ^{22}Na activation in the center foil. Sodium-22 has a half-life of 2.602 yr and decays by positron emission with a branching ratio of 90.5%. This decay produces a 1.275-MeV gamma ray with a branching ratio of 99.96%. This assessment of activation used coincidence counting techniques with the foil between two NaI crystals. These measurements, done at LANL using exactly the same technique described in Ref. 6, were made ~1 yr after the irradiations. The stability of the counting system was verified periodically using a calibrated ^{22}Na source (Amersham ID 1X967).

The proton fluence was calculated from the thickness of the aluminum foil and the cross section for production of either ^{24}Na or ^{22}Na at that particular proton energy. For the present analysis, the activation cross sections were measured in a separate experiment.[5] For the analysis in Ref. 4, existing evaluations[6–8] were used. We note that for the ^{22}Na activities, the same detector system was used in Ref. 6 for the cross-section determinations, so that particular contribution to the systematic uncertainty in the cross section did not propagate into the uncertainty of the number of protons. However, that part of the uncertainty of the cross-section determination in Ref. 5 due to measuring the beam charge is included. For the analysis here and in Ref. 4, all conversions of count rates to integrated proton fluences were done independently. There are two parts to the uncertainty associated with determining the total number of protons. The first is a statistical part due to the counting statistics and areal determinations for a given foil; the second is a systematic part due to the detector system efficiencies (1% for the ^{24}Na and 2% for the ^{22}Na) and activation cross sections (see Ref. 5).

III. RESULTS

The main purpose of this work was to provide experimental data that could be used to validate the computer codes that are used for designing and analyzing accelerator-driven spallation systems. Several spallation targets, surrounded by a tank that was filled with a $MnSO_4$ solution, were irradiated by high-energy protons. These interactions generated spallation neutrons that escaped from the target/blanket system into the tank where they were absorbed in the manganese. For this work, the actual experimental measurement that was made was the activation of the manganese. The comparisons to the code calculations were intended to show how well the computer code simulations could predict this activation. The neutron flux and energy spectra available for activating the manganese depended on the target, the blanket, the proton energy, absorption, and other neutron interactions in the target and blanket.

The various statistical and systematic uncertainties were propagated through the analysis and were combined at various points to yield the final uncertainty on the results. The statistical uncertainties from counting the various activities generally were $<1\%$. Additional systematic uncertainties arise from calibrating the counters used to measure the activation of the manganese and the aluminum, the uncertainty in the total volume of water in the system, the concentration of $MnSO_4$ in the solution, and the cross sections for proton activation of the aluminum foils. The cross sections for activation of the manganese are well characterized, and their uncertainties were negligible. The quadratic combination of all these systematic uncertainties is estimated to be 3 to 4%. These systematic uncertainties and their sources are summarized in Table II.

From the determination of the total number of ^{56}Mn atoms produced and protons delivered, the number of ^{56}Mn atoms produced per incident proton is obtained (written as $^{56}Mn/p$). This was done in two ways: One used the total number of protons determined from the measured ^{24}Na activity, and the other used the total number of protons from the measured ^{22}Na activity. Table I lists the former and latter results in columns 4 and 5, respectively. In general, agreement between the two sets of data is good. The biggest discrepancy of 10% between the measured ^{56}Mn production per proton from ^{24}Na activation and the measured ^{56}Mn production per proton from ^{22}Na activation occurred for the solid 25-cm lead target with the blanket at 400 MeV. This discrepancy is well outside the estimated uncertainties and is traceable to the aluminum activation measurements themselves. We note that where two aluminum activation measurements were made at a single proton energy and target, the result used for the ratios in Table I, column 6 is the error-weighted average of columns 4 and 5. The results in column 6 were then taken as the experimentally measured quantities for comparison with the results calculated with the LCS and MCNPX codes listed in columns 8 and 10, respectively.

IV. SIMULATIONS OF THE SYSTEM

Herein are discussed the comparisons of the experimental results with the calculated results. The results of

the calculations of the experiments listed in Table I were performed using the default combinations of models for MCNPX as discussed in Ref. 1. These results, denoted by the designation MBIP and LBIP as described below, are also shown in graphical form in Figs. 5 and 6. For the calculations in Table I, the Bertini model was used for nucleons and pions. For other particles, the ISABEL model was used. The default calculations also used the preequilibrium model after the intranuclear cascade. The highest proton energy used in the experiments was 2.0 GeV, well below the energy recommended for use of the FLUKA model, so it was never invoked. In MCNPX there are a total of 20 parametric options to choose from, some of which determine energy ranges for the models. Therefore, the total number of combinations available for any particular study is almost limitless. In this work, default energy ranges for the models were used. For the analyses of the experiments, we invoked five different model combinations (at the suggestion of a reviewer) as discussed below. For neutron interactions below 20 MeV, the ENDFB-VI evaluations as distributed with the code were used (the .60c files) wherever possible.

Table III lists the results of all the experiments normalized by the calculated results of the five model variations with both the LCS and MCNPX code systems, including the default or baseline calculations that were listed in Table I, columns 9 and 11. The results listed represent the ratios of the experimentally measured values of ^{56}Mn production per proton to the calculated values for each of the ten code calculations, i.e., $[(^{56}\mathrm{Mn}/\mathrm{p})_{measured}] \div [(^{56}\mathrm{Mn}/\mathrm{p})_{calculated}]$. These ratios are referred to as the ^{56}Mn/p ratios. An entry of unity would indicate perfect agreement between the experimental results and

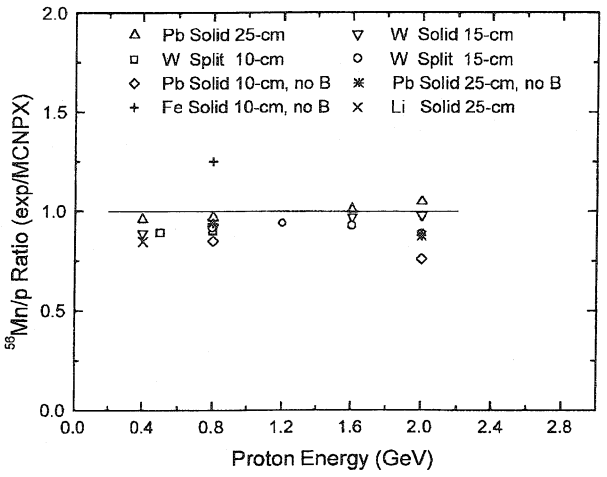

Fig. 5. Ratios of the experimentally measured values to the MCNPX-calculated values of ^{56}Mn production per proton using the Bertini-ISABEL preequilibrium model options (MBIP).

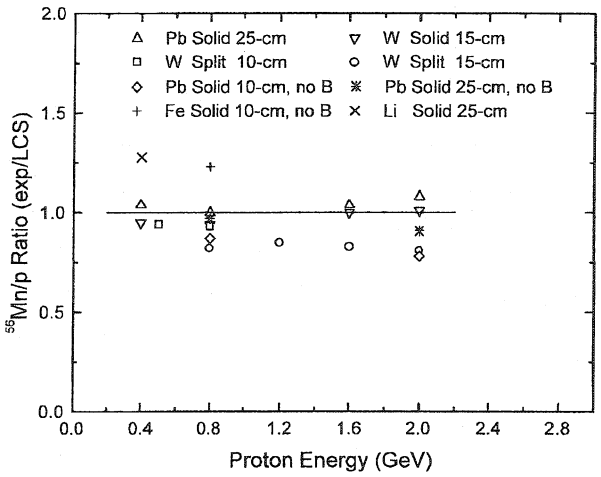

Fig. 6. Ratios of the experimentally measured values to the LCS-calculated values of ^{56}Mn production per proton using the Bertini-ISABEL preequilibrium model options (LBIP).

the calculations. The entries in Table III are posted with the acronym of the calculation that was used to normalize the indicated experimental datum. For instance, the entries for MBIP in column 3 indicate the measured values for ^{56}Mn/p production for the experiments in that column divided by the calculated results for ^{56}Mn/p production, in this case with the MCNPX code (M), using the Bertini-ISABEL model option (BI), and the preequilibrium assumption (P); thus, the entries in this column are listed as MBIP. The MCNPX calculations are denoted by M, the LCS calculations by L, the Bertini model by B, the ISABEL model by I, the Bertini-ISABEL models (BI), and with or without the preequilibrium model assumption by P or N, respectively. Since the ISABEL model is not recommended for incident particles above 1 GeV, no simulations were calculated with only the ISABEL option for experiments with proton energies >800 MeV. Calculations with only the ISABEL model are listed without discussion (Table III, columns 7 and 12)

An examination of the entries in Table III indicates several interesting trends in the ^{56}Mn/p ratios just defined. The first observation to make is that the MBIP and MBP entries in columns 3 and 5 are virtually identical. The same goes for comparisons between LBIP and LBP, MBIN and MBN, and LBIN and LBN. Furthermore, the MBIP/MBP and LBIP/LBP results are nearly identical and clearly superior to the other results. The MBIP/MBP and LBIP/LBP results indicate that these calculations on average overpredict the measured ^{56}Mn/p production by 6 to 7% for the high-Z targets (lead and tungsten). These comparisons present no incentive to choose between the MBIP, MBP, LBIP, or LBP model options for high-Z targets; the results are the same for each within stated uncertainties.

TABLE III

Ratios of the Experimentally Measured Values of ^{56}Mn Production per Proton to the Calculated Values Using the MCNPX and LCS Codes and Five Particle Transport Model Variations*

Target	Proton Energy (GeV)	^{56}Mn/p Ratio (Experiment/Calculation)									
		MBIP	MBIN	MBP	MBN	MIP	LBIP	LBIN	LBP	LBN	LIP
Solid 25 cm lead with blanket	0.4	0.96	0.91	0.97	0.91	1.00	1.04	0.98	1.05	0.99	1.07
	0.8	0.97	0.92	0.97	0.92	1.01	1.00	0.95	1.00	0.95	1.04
	0.8	0.97	0.93	0.97	0.93	1.02	1.00	0.96	1.00	0.96	1.05
	0.8	0.97	0.92	0.96	0.92	1.01	0.99	0.95	0.99	0.95	1.04
	1.6	1.01	0.98	1.01	0.98	—	1.04	1.00	1.04	1.00	—
	2.0	1.05	1.02	1.05	1.02	—	1.08	1.04	1.08	1.04	—
Solid 15 cm tungsten with blanket	0.4	0.89	0.87	0.90	0.87	0.93	0.95	0.91	0.96	0.91	0.98
	0.8	0.92	0.90	0.92	0.90	0.95	0.94	0.92	0.94	0.92	0.97
	1.6	0.97	0.95	0.97	0.95	—	1.00	0.98	1.00	0.98	—
	2.0	0.98	0.97	0.98	0.97	—	1.01	0.99	1.01	0.99	—
Split 10 cm tungsten with blanket	0.5	0.89	0.83	0.88	0.83	0.92	0.94	0.88	0.94	0.88	0.98
	0.8	0.90	0.86	0.90	0.86	0.96	0.93	0.89	0.92	0.89	0.98
Split 15 cm tungsten with blanket	0.8	0.92	0.88	0.92	0.88	0.97	0.82	0.78	0.81	0.78	0.86
	1.2	0.94	0.91	0.94	0.91	—	0.85	0.82	0.85	0.82	—
	1.6	0.93	0.90	0.93	0.90	—	0.83	0.81	0.84	0.81	—
	2.0	0.89	0.86	0.89	0.86	—	0.81	0.78	0.81	0.78	—
Solid 25 cm lead without blanket	0.8	0.94	0.87	0.94	0.87	1.00	0.97	0.90	0.97	0.90	1.03
	2.0	0.88	0.85	0.89	0.85	—	0.91	0.87	0.91	0.87	—
Solid 10 cm lead without blanket	0.8	0.85	0.78	0.85	0.78	0.93	0.87	0.80	0.87	0.80	0.96
	2.0	0.76	0.73	0.76	0.73	—	0.78	0.74	0.78	0.74	—
Solid 10 cm iron without blanket	0.8	1.25	1.22	1.25	1.21	1.47	1.23	1.20	1.23	1.20	1.55
Solid 25 cm lithium with blanket	0.4	0.85	0.80	0.85	0.80	0.89	1.28	1.22	1.28	1.22	1.45

*M, MCNPX code; L, LCS code; BIP, Bertini-ISABEL model with preequilibrium; BIN, Bertini-ISABEL model without preequilibrium; BP, Bertini model with preequilibrium; BN, Bertini model without preequilibrium; IP, ISABEL model with preequilibrium.

For the low-Z targets (iron and lithium), the comparisons in Table III are not as good as for the high-Z targets just discussed. The trends between the model variations are the same as described above for the high-Z comparisons; however, there is a peculiar difference between the LCS calculations and the MCNPX calculations. All the LCS calculations listed in Table III underpredict the measured ^{56}Mn/p production (i.e., the ^{56}Mn/p ratio is greater than unity) by 20 to 30%. However, the MCNPX calculations underpredict the iron data by as much as 25% while they overpredict the lithium data by as much as 20%. Clearly, there is a need for more work related to low-Z targets, and the analyst is cautioned to consider these results when analyzing the neutron production with low-Z targets.

The ^{56}Mn/p ratios for the solid 15-cm-diam tungsten target are closer to unity than the ^{56}Mn/p ratios for the split 15-cm-diam tungsten target. This comparison indicates that the codes are overpredicting the ^{56}Mn/p production for both solid and split configurations; however, the calculations are closer to the experimental data for the solid configuration than for the split configuration. It appears that both codes slightly overpredict the neutron leakage for the split geometry in the gaps between the segments of the target. Although this enhanced neutron leakage was the intention of the split target design for the APT, care must be taken to account for this overprediction of the neutron leakage in order to accurately predict the neutron economy in the blanket region.

The effects of target diameter on the ^{56}Mn/p production were investigated by comparing the results from the 10-cm-diam lead target and the 25-cm-diam lead target both with and without the lead blanket in place with 800-MeV and 2.0-GeV protons. In effect, lead targets with three different diameters were tested: 10-cm diameter, 25-cm diameter, and 60-cm diameter (i.e., the 25-cm-diam lead target with the lead blanket). There is good agreement between the calculations and the measurements for the 60-cm-diam lead target. However, the agreement between the calculations and the measurements for the 25-cm-diam lead target is not as good, and

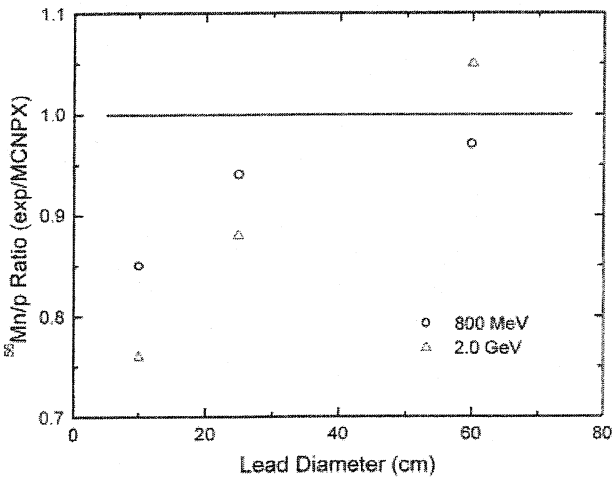

Fig. 7. Ratios of the experimentally measured values to the MCNPX-calculated values (with the MBIP model assumptions) of ^{56}Mn production per proton for three lead targets at 800 MeV and 2.0 GeV: 10-cm-diam lead target without blanket, 25-cm-diam lead target without blanket, and 25-cm lead target with blanket (= 60-cm-diam lead).

the agreement for the 10-cm-diam lead is worse. This trend is shown graphically in Fig. 7 for the three lead targets at both proton energies. The ^{56}Mn/p ratio for the 60-cm-diam lead target was approximately unity; the ^{56}Mn/p ratio for the 25-cm-diam target was ~0.9, and the ^{56}Mn/p ratio for the 10-cm-diam lead target was ~0.8. For the smaller-diameter targets, all of the calculations resulted in values for the ^{56}Mn/p production consistently higher than the measured values. The reasons for this discrepancy are complex and are not well understood at this time; any further discussion of the physical basis for these trends by the authors would be speculation.

The comparisons just presented of the experimental data to the numerical simulations demonstrate the level of accuracy of the codes in predicting the total neutron production (as inferred through manganese activation per proton) over a range of target materials and configurations, and for a range of proton energies. The LCS and MCNPX code simulations using the MCNPX default model options (MBIP and LBIP) generally overpredict the measured manganese activation per proton for the high-Z targets (lead and tungsten) by 6 to 7%, whereas the simulations for the low-Z targets (lithium and iron) are not nearly as good. Low-Z targets warrant further investigation.

ACKNOWLEDGMENTS

This work was performed under contract W-7405-ENG-36 with the U.S. Department of Energy.

REFERENCES

1. "MCNPX™ User's Manual, Version 2.3.0," LA-UR-02-2007, L. S. WATERS, Ed., Los Alamos National Laboratory (2002).

2. R. E. PRAEL and H. LICHTENSTEIN, LA-UR-89-3014, Los Alamos National Laboratory (1989).

3. G. L. MORGAN, G. BUTLER, M. CAPPIELLO, S. CARIUS, L. DAEMEN, B. DEVOLDER, J. FREHAUT, C. GOULDING, R. GRACE, R. GREEN, P. LISOWSKI, P. E. LITTLETON, J. KING, N. S. P. KING, R. PRAEL, T. STRATTON, S. TURNER, J. ULLMANN, F. VENNERI, and M. YATES, "LANL Sunnyside Experiment: Study of Neutron Production in Accelerator-Driven Targets," *Accelerator-Driven Transmutation Technologies and Applications, AIP Conf. Proc.*, **346**, 682 (1994).

4. J. FREHAUT, D. DENEUVILLE, X. LEDOUX, J. P. LOCHARD, J. L. LONGUET, E. PETIBON, K. R. ALRICK, D. W. BOWMAN, F. C. CVERNA, N. S. P. KING, G. L. MORGAN, G. A. GREENE, A. L. HANSON, C. L. SNEAD, Jr., E. A. HENRY, R. T. THOMPSON, and T. E. WARD, "Measure Integrale de la Production de Neutrons dans des Cibles de Spallation," CEA-R-5809, Commissariat à l'Energie Atomique (1998).

5. G. L. MORGAN, K. R. ALRICK, A. SAUNDERS, F. C. CVERNA, N. S. P. KING, F. E. MERRILL, L. S. WATERS, A. L. HANSON, G. A. GREENE, R. P. LILJESTRAND, R. T. THOMPSON, and E. A. HENRY, *Nucl. Instrum. Methods B*, **211**, *3*, 297 (2003).

6. T. N. TADDEUCCI, J. ULLMANN, L. J. RYBARCYK, G. W. BUTLER, and T. E. WARD, *Phys. Rev. C*, **55**, 1551 (1963).

7. J. B. CUMMING, *Ann. Rev. Nucl. Sci.*, **13**, 261 (1963).

8. J. TOBAILEM, C. H. DE LASSUS ST. GENIES, and I. LEVEQUE, CEA-N-1466 (5), Centre d'Etudes Nucleaires de Saclay (1981).

9. G. L. MORGAN, Personal Communication (1994).